Deviation from quark number scaling of the anisotropy parameter v(2) of pions, kaons, and protons in Au+Au collisions at root s(NN)=200 GeV

Adare, A.; Afanasiev, S.; Aidala, C.; Ajitanand, N. N.; Akiba, Y.; Al-Bataineh, H.; Alexander, J.; Aoki, K.; Aramaki, Y.; Atomssa, E. T.; Averbeck, R.; Awes, T. C.; Azmoun, B.; Babintsev, V.; Bai, M.; Baksay, G.; Baksay, L.; Barish, K. N.; Bassalleck, B.; Basye, A. T.; Bathe, S.; Baublis, V.; Baumann, C.; Bazilevsky, A.; Belikov, S.; Belmont, R.; Bennett, R.; Berdnikov, A.; Berdnikov, Y.; Bickley, A. A.; Bok, J. S.; Boyle, K.; Brooks, M. L.; Buesching, H.; Bumazhnov, V.; Bunce, G.; Butsyk, S.; Camacho, C. M.; Campbell, S.; Chen, C. -H.; Chi, C. Y.; Chiu, M.; Choi, I. J.; Choudhury, R. K.; Christiansen, Peter; Chujo, T.; Chung, P.; Chvala, O.; Cianciolo, V.; Citron, Z.

Published in:
Physical Review C (Nuclear Physics)

DOI:
10.1103/PhysRevC.85.064914

2012

Deviation from quark number scaling of the anisotropy parameter v_2 of pions, kaons, and protons in Au + Au collisions at $\sqrt{s_{NN}} = 200$ GeV

A. Adare,[11] S. Afanasiev,[27] C. Aidala,[39] N. N. Ajitanand,[56] Y. Akiba,[50,51] H. Al-Bataineh,[45] J. Alexander,[56] K. Aoki,[32,50] Y. Aramaki,[10] E. T. Atomssa,[33] R. Averbeck,[57] T. C. Awes,[46] B. Azmoun,[5] V. Babintsev,[22] M. Bai,[4] G. Baksay,[18] L. Baksay,[18] K. N. Barish,[6] B. Bassalleck,[44] A. T. Basye,[1] S. Bathe,[6] V. Baublis,[49] C. Baumann,[40] A. Bazilevsky,[5] S. Belikov,[5,*] R. Belmont,[61] R. Bennett,[57] A. Berdnikov,[53] Y. Berdnikov,[53] A. A. Bickley,[11] J. S. Bok,[65] K. Boyle,[57] M. L. Brooks,[35] H. Buesching,[5] V. Bumazhnov,[22] G. Bunce,[5,51] S. Butsyk,[35] C. M. Camacho,[35] S. Campbell,[57] C.-H. Chen,[57] C. Y. Chi,[12] M. Chiu,[5] I. J. Choi,[65] R. K. Choudhury,[3] P. Christiansen,[37] T. Chujo,[60] P. Chung,[56] O. Chvala,[6] V. Cianciolo,[46] Z. Citron,[57] B. A. Cole,[12] M. Connors,[57] P. Constantin,[35] M. Csanád,[16] T. Csörgő,[64] T. Dahms,[57] S. Dairaku,[32,50] I. Danchev,[61] K. Das,[19] A. Datta,[39] G. David,[5] A. Denisov,[22] A. Deshpande,[51,57] E. J. Desmond,[5] O. Dietzsch,[54] A. Dion,[57] M. Donadelli,[54] O. Drapier,[33] A. Drees,[57] K. A. Drees,[4] J. M. Durham,[57] A. Durum,[22] D. Dutta,[3] S. Edwards,[19] Y. V. Efremenko,[46] F. Ellinghaus,[11] T. Engelmore,[12] A. Enokizono,[34] H. En'yo,[50,51] S. Esumi,[60] B. Fadem,[41] D. E. Fields,[44] M. Finger,[7] M. Finger Jr.,[7] F. Fleuret,[33] S. L. Fokin,[31] Z. Fraenkel,[63,*] J. E. Frantz,[57] A. Franz,[5] A. D. Frawley,[19] K. Fujiwara,[50] Y. Fukao,[50] T. Fusayasu,[43] I. Garishvili,[58] A. Glenn,[11] H. Gong,[57] M. Gonin,[33] Y. Goto,[50,51] R. Granier de Cassagnac,[33] N. Grau,[12] S. V. Greene,[61] M. Grosse Perdekamp,[23,51] T. Gunji,[10] H.-Å. Gustafsson,[37,*] J. S. Haggerty,[5] K. I. Hahn,[17] H. Hamagaki,[10] J. Hamblen,[58] R. Han,[48] J. Hanks,[12] E. P. Hartouni,[34] E. Haslum,[37] R. Hayano,[10] X. He,[20] M. Heffner,[34] T. K. Hemmick,[57] T. Hester,[6] J. C. Hill,[26] M. Hohlmann,[18] W. Holzmann,[12] K. Homma,[21] B. Hong,[30] T. Horaguchi,[21] D. Hornback,[58] S. Huang,[61] T. Ichihara,[50,51] R. Ichimiya,[50] J. Ide,[41] Y. Ikeda,[60] K. Imai,[32,50] M. Inaba,[60] D. Isenhower,[1] M. Ishihara,[50] T. Isobe,[10,50] M. Issah,[61] A. Isupov,[27] D. Ivanischev,[49] B. V. Jacak,[57,†] J. Jia,[5,56] J. Jin,[12] B. M. Johnson,[5] K. S. Joo,[42] D. Jouan,[47] D. S. Jumper,[1] F. Kajihara,[10] S. Kametani,[50] N. Kamihara,[51] J. Kamin,[57] J. H. Kang,[65] J. Kapustinsky,[35] K. Karatsu,[32,50] D. Kawall,[39,51] M. Kawashima,[50,52] A. V. Kazantsev,[31] T. Kempel,[26] A. Khanzadeev,[49] K. M. Kijima,[21] B. I. Kim,[30] D. H. Kim,[42] D. J. Kim,[28] E. Kim,[55] E. J. Kim,[8] S. H. Kim,[65] Y. J. Kim,[23] E. Kinney,[11] K. Kiriluk,[11] Á. Kiss,[16] E. Kistenev,[5] L. Kochenda,[49] B. Komkov,[49] M. Konno,[60] J. Koster,[23] D. Kotchetkov,[44] A. Kozlov,[63] A. Král,[13] A. Kravitz,[12] G. J. Kunde,[35] K. Kurita,[50,52] M. Kurosawa,[50] Y. Kwon,[65] G. S. Kyle,[45] R. Lacey,[56] Y. S. Lai,[12] J. G. Lajoie,[26] A. Lebedev,[26] D. M. Lee,[35] J. Lee,[17] K. Lee,[55] K. B. Lee,[30] K. S. Lee,[30] M. J. Leitch,[35] M. A. L. Leite,[54] E. Leitner,[61] B. Lenzi,[54] X. Li,[9] P. Liebing,[51] L. A. Linden Levy,[11] T. Liška,[13] A. Litvinenko,[27] H. Liu,[35,45] M. X. Liu,[35] B. Love,[61] R. Luechtenborg,[40] D. Lynch,[5] C. F. Maguire,[61] Y. I. Makdisi,[4] A. Malakhov,[27] M. D. Malik,[44] V. I. Manko,[31] E. Mannel,[12] Y. Mao,[48,50] H. Masui,[60] F. Matathias,[12] M. McCumber,[57] P. L. McGaughey,[35] N. Means,[57] B. Meredith,[23] Y. Miake,[60] A. C. Mignerey,[38] P. Mikeš,[7,25] K. Miki,[50,60] A. Milov,[5] M. Mishra,[2] J. T. Mitchell,[5] A. K. Mohanty,[3] Y. Morino,[10] A. Morreale,[6] D. P. Morrison,[5] T. V. Moukhanova,[31] J. Murata,[50,52] S. Nagamiya,[29] J. L. Nagle,[11] M. Naglis,[63] M. I. Nagy,[16] I. Nakagawa,[50,51] Y. Nakamiya,[21] T. Nakamura,[21,29] K. Nakano,[50,59] J. Newby,[34] M. Nguyen,[57] R. Nouicer,[5] A. S. Nyanin,[31] E. O'Brien,[5] S. X. Oda,[10] C. A. Ogilvie,[26] M. Oka,[60] K. Okada,[51] Y. Onuki,[50] A. Oskarsson,[37] M. Ouchida,[21,50] K. Ozawa,[10] R. Pak,[5] V. Pantuev,[24,57] V. Papavassiliou,[45] I. H. Park,[17] J. Park,[55] S. K. Park,[30] W. J. Park,[30] S. F. Pate,[45] H. Pei,[26] J.-C. Peng,[23] H. Pereira,[14] V. Peresedov,[27] D. Yu. Peressounko,[31] C. Pinkenburg,[5] R. P. Pisani,[5] M. Proissl,[57] M. L. Purschke,[5] A. K. Purwar,[35] H. Qu,[20] J. Rak,[28] A. Rakotozafindrabe,[33] I. Ravinovich,[63] K. F. Read,[46,58] K. Reygers,[40] V. Riabov,[49] Y. Riabov,[49] E. Richardson,[38] D. Roach,[61] G. Roche,[36] S. D. Rolnick,[6] M. Rosati,[26] C. A. Rosen,[11] S. S. E. Rosendahl,[37] P. Rosnet,[36] P. Rukoyatkin,[27] P. Ružička,[25] B. Sahlmueller,[40] N. Saito,[29] T. Sakaguchi,[5] K. Sakashita,[50,59] V. Samsonov,[49] S. Sano,[10,62] T. Sato,[60] S. Sawada,[29] K. Sedgwick,[6] J. Seele,[11] R. Seidl,[23] A. Yu. Semenov,[26] R. Seto,[6] D. Sharma,[63] I. Shein,[22] T.-A. Shibata,[50,59] K. Shigaki,[21] M. Shimomura,[60] K. Shoji,[32,50] P. Shukla,[3] A. Sickles,[5] C. L. Silva,[54] D. Silvermyr,[46] C. Silvestre,[14] K. S. Sim,[30] B. K. Singh,[2] C. P. Singh,[2] V. Singh,[2] M. Slunečka,[7] R. A. Soltz,[34] W. E. Sondheim,[35] S. P. Sorensen,[58] I. V. Sourikova,[5] N. A. Sparks,[1] P. W. Stankus,[46] E. Stenlund,[37] S. P. Stoll,[5] T. Sugitate,[21] A. Sukhanov,[5] J. Sziklai,[64] E. M. Takagui,[54] A. Taketani,[50,51] R. Tanabe,[60] Y. Tanaka,[43] K. Tanida,[32,50,51] M. J. Tannenbaum,[5] S. Tarafdar,[2] A. Taranenko,[56] P. Tarján,[15] H. Themann,[57] T. L. Thomas,[44] M. Togawa,[32,50] A. Toia,[57] L. Tomášek,[25] H. Torii,[21] R. S. Towell,[1] I. Tserruya,[63] Y. Tsuchimoto,[21] C. Vale,[5,26] H. Valle,[61] H. W. van Hecke,[35] E. Vazquez-Zambrano,[12] A. Veicht,[23] J. Velkovska,[61] R. Vértesi,[15,64] A. A. Vinogradov,[31] M. Virius,[13] V. Vrba,[25] E. Vznuzdaev,[49] X. R. Wang,[45] D. Watanabe,[21] K. Watanabe,[60] Y. Watanabe,[50,51] F. Wei,[26] R. Wei,[56] J. Wessels,[40] S. N. White,[5] D. Winter,[12] J. P. Wood,[1] C. L. Woody,[5] R. M. Wright,[1] M. Wysocki,[11] W. Xie,[51] Y. L. Yamaguchi,[10] K. Yamaura,[21] R. Yang,[23] A. Yanovich,[22] J. Ying,[20] S. Yokkaichi,[50,51] Z. You,[48] G. R. Young,[46] I. Younus,[44] I. E. Yushmanov,[31] W. A. Zajc,[12] C. Zhang,[46] S. Zhou,[9] and L. Zolin[27]

(PHENIX Collaboration)

[1]*Abilene Christian University, Abilene, Texas 79699, USA*

[2]*Department of Physics, Banaras Hindu University, Varanasi 221005, India*

[3]*Bhabha Atomic Research Centre, Bombay 400 085, India*

[4]*Collider-Accelerator Department, Brookhaven National Laboratory, Upton, New York 11973-5000, USA*

[5]*Physics Department, Brookhaven National Laboratory, Upton, New York 11973-5000, USA*

[6]*University of California - Riverside, Riverside, California 92521, USA*

[7]*Charles University, Ovocný trh 5, Praha 1, 116 36 Prague, Czech Republic*

[8]*Chonbuk National University, Jeonju 561-756, Korea*

[9]*Science and Technology on Nuclear Data Laboratory, China Institute of Atomic Energy, Beijing 102413, People's Republic of China*
[10]*Center for Nuclear Study, Graduate School of Science, University of Tokyo, 7-3-1 Hongo, Bunkyo, Tokyo 113-0033, Japan*
[11]*University of Colorado, Boulder, Colorado 80309, USA*
[12]*Columbia University, New York, New York 10027 and Nevis Laboratories, Irvington, New York 10533, USA*
[13]*Czech Technical University, Zikova 4, 166 36 Prague 6, Czech Republic*
[14]*Dapnia, Commissariat à l'Énergie Atomique - Saclay, F-91191 Gif-sur-Yvette, France*
[15]*Debrecen University, H-4010 Debrecen, Egyetem tér 1, Hungary*
[16]*ELTE, Eötvös Loránd University, H-1117 Budapest, Pázmány P. s. 1/A, Hungary*
[17]*Ewha Womans University, Seoul 120-750, Korea*
[18]*Florida Institute of Technology, Melbourne, Florida 32901, USA*
[19]*Florida State University, Tallahassee, Florida 32306, USA*
[20]*Georgia State University, Atlanta, Georgia 30303, USA*
[21]*Hiroshima University, Kagamiyama, Higashi-Hiroshima 739-8526, Japan*
[22]*IHEP Protvino, State Research Center of Russian Federation, Institute for High Energy Physics, Protvino 142281, Russia*
[23]*University of Illinois at Urbana - Champaign, Urbana, Illinois 61801, USA*
[24]*Institute for Nuclear Research of the Russian Academy of Sciences, prospekt 60-letiya Oktyabrya 7a, Moscow 117312, Russia*
[25]*Institute of Physics, Academy of Sciences of the Czech Republic, Na Slovance 2, 182 21 Prague 8, Czech Republic*
[26]*Iowa State University, Ames, Iowa 50011, USA*
[27]*Joint Institute for Nuclear Research, 141980 Dubna, Moscow Region, Russia*
[28]*Helsinki Institute of Physics and University of Jyväskylä, P.O. Box 35, FI-40014 Jyväskylä, Finland*
[29]*KEK, High Energy Accelerator Research Organization, Tsukuba, Ibaraki 305-0801, Japan*
[30]*Korea University, Seoul 136-701, Korea*
[31]*Russian Research Center "Kurchatov Institute", Moscow 123098, Russia*
[32]*Kyoto University, Kyoto 606-8502, Japan*
[33]*Laboratoire Leprince-Ringuet, Ecole Polytechnique, CNRS-IN2P3, Route de Saclay, F-91128 Palaiseau, France*
[34]*Lawrence Livermore National Laboratory, Livermore, California 94550, USA*
[35]*Los Alamos National Laboratory, Los Alamos, New Mexico 87545, USA*
[36]*Laboratoire de Phyisique Corpusculaire, Université Blaise Pascal, CNRS-IN2P3, Clermont-Fd, 63177 Aubiere Cedex, France*
[37]*Department of Physics, Lund University, Box 118, SE-221 00 Lund, Sweden*
[38]*University of Maryland, College Park, Maryland 20742, USA*
[39]*Department of Physics, University of Massachusetts, Amherst, Massachusetts 01003-9337, USA*
[40]*Institut fur Kernphysik, University of Muenster, D-48149 Muenster, Germany*
[41]*Muhlenberg College, Allentown, Pennsylvania 18104-5586, USA*
[42]*Myongji University, Yongin, Kyonggido 449-728, Korea*
[43]*Nagasaki Institute of Applied Science, Nagasaki-shi, Nagasaki 851-0193, Japan*
[44]*University of New Mexico, Albuquerque, New Mexico 87131, USA*
[45]*New Mexico State University, Las Cruces, New Mexico 88003, USA*
[46]*Oak Ridge National Laboratory, Oak Ridge, Tennessee 37831, USA*
[47]*Institut de Physique Nucléaire - Orsay, Universite Paris Sud, CNRS-IN2P3, BP1, F-91406 Orsay, France*
[48]*Peking University, Beijing 100871, People's Republic of China*
[49]*PNPI, Petersburg Nuclear Physics Institute, Gatchina, Leningrad region 188300, Russia*
[50]*RIKEN Nishina Center for Accelerator-Based Science, Wako, Saitama 351-0198, Japan*
[51]*RIKEN BNL Research Center, Brookhaven National Laboratory, Upton, New York 11973-5000, USA*
[52]*Physics Department, Rikkyo University, 3-34-1 Nishi-Ikebukuro, Toshima, Tokyo 171-8501, Japan*
[53]*Saint Petersburg State Polytechnic University, St. Petersburg 195251, Russia*
[54]*Universidade de São Paulo, Instituto de Física, Caixa Postal 66318, São Paulo CEP05315-970, Brazil*
[55]*Seoul National University, Seoul, Korea*
[56]*Chemistry Department, Stony Brook University, State University of New York, Stony Brook, New York 11794-3400, USA*
[57]*Department of Physics and Astronomy, Stony Brook University, State University of New York, Stony Brook, New York 11794-3400, USA*
[58]*University of Tennessee, Knoxville, Tennessee 37996, USA*
[59]*Department of Physics, Tokyo Institute of Technology, Oh-okayama, Meguro, Tokyo 152-8551, Japan*
[60]*Institute of Physics, University of Tsukuba, Tsukuba, Ibaraki 305, Japan*
[61]*Vanderbilt University, Nashville, Tennessee 37235, USA*
[62]*Waseda University, Advanced Research Institute for Science and Engineering, 17 Kikui-cho, Shinjuku-ku, Tokyo 162-0044, Japan*

[63]Weizmann Institute, Rehovot 76100, Israel
[64]Institute for Particle and Nuclear Physics, Wigner Research Centre for Physics, Hungarian Academy of Sciences (Wigner RCP, RMKI) H-1525 Budapest 114, P.O. Box 49, Budapest, Hungary
[65]Institute of Physics and Applied Physics, Yonsei University, Seoul 120-749, Korea
(Received 12 March 2012; published 25 June 2012)

Measurements of the anisotropy parameter v_2 of identified hadrons (pions, kaons, and protons) as a function of centrality, transverse momentum p_T, and transverse kinetic energy KE_T at midrapidity ($|\eta| < 0.35$) in Au + Au collisions at $\sqrt{s_{NN}} = 200$ GeV are presented. Pions and protons are identified up to $p_T = 6$ GeV/c, and kaons up to $p_T = 4$ GeV/c, by combining information from time-of-flight and aerogel Čerenkov detectors in the PHENIX Experiment. The scaling of v_2 with the number of valence quarks (n_q) has been studied in different centrality bins as a function of transverse momentum and transverse kinetic energy. A deviation from previously observed quark-number scaling is observed at large values of KE_T/n_q in noncentral Au + Au collisions (20–60%), but this scaling remains valid in central collisions (0–10%).

DOI: 10.1103/PhysRevC.85.064914 PACS number(s): 25.75.Dw, 25.75.Ld

I. INTRODUCTION

Measurements of the anisotropy parameter v_2 (the second coefficient in the Fourier expansion of the hadron yields with respect to the reaction plane) have played a pivotal role in the discovery of the strongly coupled quark-gluon plasma (sQGP) at RHIC [1–4]. At low p_T ($\leqslant$2 GeV/c) the agreement between ideal hydrodynamics calculations and the data have led to the conclusion that a near-perfect fluid is created in heavy-ion collisions at RHIC [5,6]. Recent theoretical efforts aiming to quantify the ratio of the shear viscosity to the entropy density η/s (see, for example, reviews in Refs. [7–9]) have confirmed that in the sQGP fluid this ratio is close to a conjectured quantum limit [10]. The high p_T ($\geqslant$6 GeV/c) azimuthal anisotropies [11–13] have been attributed to the path-length dependence of energy loss in the medium and are used to constrain the theoretical descriptions of jet energy loss [14,15]. At intermediate p_T (2–6 GeV/c), which is the focus of this paper, the identified hadron anisotropies have shown strong evidence for quarklike degrees of freedom and significant collectivity at the parton level. This is supported by the observation of scaling with the number of valence quarks in the hadron (n_q scaling) [16–21].

The scaling with number of valence quarks (n_q) was seen as a confirmation of quark recombination as a particle-production mechanism that competes with fragmentation in the intermediate-p_T range. Recombination models [22–26] were developed to account for the unusually large baryon-to-meson ratios (relative to $p + p$ collisions) and nuclear-modification factors [17,27,28], as well as the large elliptic flow at intermediate p_T, with pronounced differences between baryons and mesons. In the models, the n_q scaling, which is manifested as $v_2^{\mathrm{hadron}}(p_T) \approx n_q v_2(p_T/n_q)$, is an approximate scaling that comes from the addition of the valence-quark momenta at hadronization, with the assumption that the collective flow develops at the partonic level.

There are several theoretical considerations that suggest that the n_q scaling should be violated in certain conditions. For example, the inclusion of higher Fock states describing the contribution of sea quarks and gluons have been shown to affect the n_q scaling [29]. Similarly, models that consider recombination between "thermal" partons (soft partons thermalized in the medium) and "shower" partons (partons fragmented from jets) predict centrality-dependent deviations from n_q scaling that are particle-species dependent [30]. Understanding the limits of the recombination domain is important in relation to viscous hydrodynamics and the extraction of the shear viscosity over entropy density (η/s) from the data [31–33], as well as for developing a unified approach in describing jet energy loss and high $p_T v_2$ [34–36]. Searches for deviations from n_q scaling are also important for the low-energy scan program at RHIC as they have been considered as a signature of the transition between sQGP formation and a hadronic system. Recent considerations of baryon transport may complicate this picture [37], which further reinforces the need for a detailed understanding of this scaling at $\sqrt{s_{NN}} = 200$ GeV.

The n_q scaling has been tested in certain centralities and p_T regions with identified particles [16–21]. However, the precision of experimental data on identified hadron v_2 is in many cases limited in statistics and p_T reach, especially for baryon measurements at $\mathrm{KE}_T/n_q > 1$ GeV ($\mathrm{KE}_T = \sqrt{p_T^2 + m_0^2} - m_0$) where the n_q scaling may start to break. Therefore, the detailed p_T limits and centrality dependence of the n_q scaling have not been tested.

This paper reports on high-statistics measurements of the second-order Fourier coefficient v_2 for identified pions ($\pi^+ + \pi^-$), kaons ($K^+ + K^-$), and protons ($p + \bar{p}$), which extend to relatively high p_T (up to 6 GeV/c for pions and protons and 4 GeV/c for kaons). The data for different centrality events (0–10%, 10–20%, 20–40%, 40–60%, and combinations thereof) are analyzed separately and the n_q scaling is examined as a function of centrality. Comparisons with published measurements of K^0_S and Λ from STAR Collaboration [21] are shown in the centralities 0–10% and 10–40%. The experimental details are presented in Sec. II, the analysis methods are in Sec. III, the results

*Deceased.
†PHENIX Spokesperson: jacak@skipper.physics.sunysb.edu

and discussion are in Secs. IV and V summarizes our findings.

II. EXPERIMENTAL SETUP

The PHENIX experiment is designed for the study of nuclear matter in extreme conditions through a variety of experimental observables. It comprises a tracking system optimized for the high-multiplicity environment of ultrarelativistic heavy-ion collisions, a set of particle identification (PID) detectors, and a set of detectors aimed at determining the global properties of the collisions.

Figure 1 shows a schematic diagram of the PHENIX detector. The upper part is a beam-axis view of the two central spectrometer arms (West and East), covering the pseudorapidity region of $|\eta| < 0.35$. Below that is a side view showing the two forward-rapidity muon arms (South and North) and the global detectors. A detailed description of the complete set of detectors can be found elsewhere [38].

The physics analysis presented here employed the tracking system [drift chamber (DC) and three layers of multiwire proportional chambers (PC1, PC2, and PC3)], the West arm time-of-flight detector (TOFw), the aerogel Čerenkov counter (ACC), the ring imaging Čerenkov counter (RICH), the beam-beam counters (BBC), the reaction-plane detector (RxNP), and the muon piston calorimeter (MPC). Below, we give a brief description of each of these detector subsystems and their role in the present analysis.

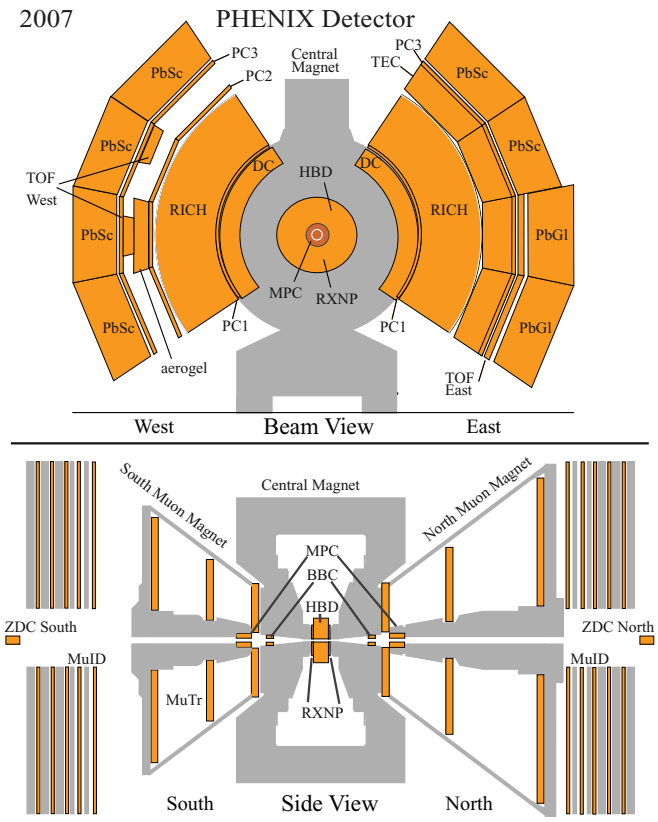

FIG. 1. (Color online) The PHENIX detector configuration for RHIC 2007 data-taking period. The West arm time-of-flight detector (TOFw) is labeled as TOF West.

A. Global detectors

The BBCs are located at ± 144 cm from the nominal interaction point along the beam line in the pseudorapidity region $3.0 < |\eta| < 3.9$. Each BBC comprises 64 Čerenkov telescopes, arranged radially around the beam line. The BBCs provide the main collision trigger for the experiment and are used in the determination of the collision vertex position along the beam axis (z vertex) and the centrality of the collisions. They also provide the start time for the time-of-flight measurement with timing resolution of $\sigma_{\mathrm{BBC}} = 37$ ps.

The RxNP [39] was installed in PHENIX before the 2007 data-taking period. It is located at ± 38 cm from the nominal interaction point and has full azimuthal coverage. Each RxNP comprises two rings of plastic scintillator paddles, with each paddle subtending $\Delta\phi = \pi/6$. The inner and outer segments cover the pseudorapidity ranges $1.0 < |\eta| < 1.5$ and $1.5 < |\eta| < 2.8$, respectively. The RxNP is the main detector used in the event-plane determination for this analysis. The event-plane resolution [Res(Ψ)] [40], which is used as a correction to the v_2 measurement, is defined as

$$\mathrm{Res}(\Psi) = \langle \cos[2(\Psi - \Psi_{\mathrm{RP}})] \rangle. \quad (1)$$

Here the bracket $\langle\rangle$ indicates an average over all events, Ψ_{RP} is the true reaction plane (which is defined by the directions of interaction parameter and beam), and Ψ is the event plane (which is measured by the detector event by event). A larger value of Res(Ψ) corresponds to a better measurement of the event plane. In a given event, the event-plane resolution depends on the charged-particle multiplicity and the size of the azimuthal anisotropy signal; thus the resolution is centrality dependent. A resolution of up to 73% is achieved for midcentral events.

The MPCs are electromagnetic calorimeters situated at ± 223 cm from the nominal interaction point inside the cylindrical openings at the front of the muon magnet pistons [41] and have 2π azimuthal acceptance. The pseudorapidity coverage is about $3.0 < \eta < 3.8$ for the north side and $-3.7 < \eta < -3.1$ for the south side. The MPCs are comprised of 220 modules in the north piston hole and 192 in the south with $PbWO_4$ crystals and Avalanche Photodiode readouts, and can detect both charged and neutral particles. In this analysis, the MPCs were used for event-plane determination. Although the event-plane resolution (up to 50% in midcentral collisions) is lower than that achieved with the RxNP, the MPCs provide an important systematic check on the RxNP measurement due to their larger pseudorapidity separation from the central spectrometer and therefore smaller nonflow effects on the v_2 measurement.

B. Tracking and particle identification detectors

The charged-particle momentum is reconstructed in the tracking system comprised of the DC located outside of an axially symmetric magnetic field at a radial distance between 2.0 m and 2.4 m followed by the PC1 with pixel-pad readout.

The pattern recognition in the DC is based on a combinatorial Hough transform in the track bend plane. A track model based on a field-integral lookup table determines the charged-particle momentum, the path length to the TOFw, and a projection of the track to the outer detectors. The momentum resolution in this data set was estimated to be $\delta p/p \approx 1.3\% \oplus 1.2\% \times p$ (GeV/c), where the first term represents multiple scattering up to the DC and the second term is due to the DC spatial resolution. The momentum resolution is worse than previous data sets, because the bucked field of the PHENIX central magnet provided less than half the magnetic field strength of the standard configuration [42].

The tracks are matched to hits registered in the second and third layers of the pad chambers, PC2 and PC3, which are located at radial distances of 4.19 m and 4.98 m from the interaction point. Thus, the contribution of tracks originating from decays and γ conversions is reduced.

To improve the track purity further, we employ the RICH, which is a threshold gas Čerenkov detector located in the radial region 2.5 m $< r <$ 4.1 m. The Čerenkov radiator gas (CO_2) at atmospheric pressure has an index of refraction $n = 1.000410$ ($\gamma_{\text{th}} = 35$), which corresponds to a momentum threshold of 20 MeV/c for an electron and 4.65 GeV/c for a pion. The RICH provides a veto for the electrons and positrons, which are predominantly pairs resulting from γ conversions and Dalitz decays.

The primary PID used in this analysis is the TOFw, which is located at a radial distance of 4.81 m from the interaction point and covers the pseudorapidity range $|\eta| < 0.35$ and $\delta\phi = 22^\circ$ in azimuth. The TOFw was built using multigap resistive plate chamber technology (MRPC) [43] and installed in PHENIX before the 2007 data-taking period. The MRPCs have six gas gaps formed by layered glass plates with thickness of 550 μm, separated by 230 μm-thick monofilament fishing line. The MRPCs are positioned in a gas volume and operated with a gas mixture of 95% R134a and 5% isobutane (C_4H_{10}), and bias voltage of 14 kV. The TOFw system is composed of 128 MRPC modules each of which has four signal strips of size 37 $\times$ 2.8 cm^2 and separation of 0.3 cm. The readout [44] is double sided, which allows for hit positioning along the direction of the strip to be determined using the timing difference between the signals with resolution of the order 1 cm. The other two hit coordinates are determined using the global position of the strips within PHENIX. The average time measured on both sides of the strips provides the stop time for the time-of-flight measurement. The timing resolution of the BBC-TOFw system was determined by selecting charged tracks (see Sec. III A) with momentum in the range 1.1 GeV/$c < p <$ 1.5 GeV/c and examining the timing difference between the measured flight time and the time that is expected under the assumption that the particles are pions. The resulting time distribution is shown in Fig. 2. Since the pions dominate the total yield in this momentum region, a narrow peak centered around $t - t_{\text{expected}} \approx 0$ is observed. The other two broad peaks in Fig. 2 correspond to kaons and protons. A Gaussian distribution is fit to the pion peak and yields a resolution of $\sigma_{\text{BBC-TOFw}} = 84 \pm 1$ ps for the BBC-TOFw system.

The excellent timing resolution allows for 4σ separation in mass-squared reaching up to $p_T = 2.5$ GeV/c for π/K, and up to $p_T = 4$ GeV/c for K/p. The PID is further extended in p_T by use of asymmetric cuts around the centroids of the mass-squared distributions.

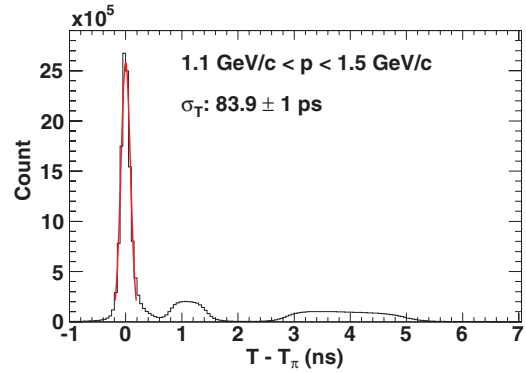

FIG. 2. (Color online) Timing difference $T - T_\pi$, the difference between the measured time in the TOFw and the time calculated assuming each candidate track is a pion.

The ACC is used in conjunction with the TOFw to aid the PID at high p_T. It is situated in the West spectrometer arm in front of the TOFw detector. The ACC is a Čerenkov radiation detector with a relatively high index of refraction ($n = 1.0113$, $\gamma_{\text{th}} = 8.5$), which means that light is produced at relatively low momenta. The threshold for radiation is 1.0 GeV/c for pions, 3.0 GeV/c for kaons, and 6.0 GeV/c for protons. The combined ACC-TOFw information allows for π/K separation up to $p_T = 4$ GeV/c, and K/p separation up to $p_T = 6$ GeV/c. The main characteristic parameters of TOFw and ACC can be found in the Table I.

III. ANALYSIS METHOD

A. Event and track selection

The results reported here are obtained from an analysis of 4.8×10^9 minimum bias events obtained during the 2007 running period. The minimum-bias trigger is defined by a coincidence between North and South BBC signals and an energy threshold of one neutron in both the North and South zero-degree calorimeters [38]. The collision vertex z is constrained to $|z| < 30$ cm of the origin of the coordinate system.

Charged tracks are selected based on the track quality information from the tracking system (DC-PC1). The tracks are then projected to the outer detectors and confirmed by requiring that the closest hit to the track projection is within certain spatial windows in ϕ and z. The distributions for

TABLE I. The main characteristic parameters of TOFw and ACC.

	TOFw	ACC
$\Delta\eta$	$(-0.35, 0.35)$	$(-0.35, 0.35)$
$\Delta\phi$ (rad)	$(-0.061, 0.110)$ $(0.503, 0.674)$	$(-0.108, 0.156)$
Radial distance (cm)	481.36	449.4
Number of cells	512	160
Cell size (cm^2)	37×2.8	11.95×23.10

the distance between the closest hit and projection in the azimuthal and z directions are fitted with a double-Gaussian function, one Gaussian function is for the signal distribution and the other for the background. For $p_T < 3$ GeV/c, hits are required to match the TOFw and the PC3 to within 2σ from the signal's Gaussian distribution in ϕ and z. For $p_T \geqslant 3$ GeV/c, hits are required to match the PC2 and the PC3 to within 3σ and the TOFw to within 2σ in ϕ and z. Background from γ conversions is further reduced by applying a RICH veto. For the pions, this veto only works for $p_T < 5$ GeV/c since pions with p_T higher than that will fire the RICH. To evaluate the residual background, remaining after these selections, the background-to-signal (B/S) ratios from the double-Gaussian function fitting within the samples selected for the analysis are examined. For $p_T < 3$ GeV/c the background comprises less than 1% of the selected tracks. At higher p_T the background increases, reaching B/S $\approx 7\%$ for 5.5 GeV/c $< p_T <$ 6.0 GeV/c in the 0–20% centrality bin.

B. Particle identification

The particles are identified by their mass, based on measurements of the momentum, the time-of-flight to the TOFw detector, and the path length along the trajectory. PID selections are performed by applying momentum-dependent cuts in mass-squared. The mass-squared distributions are fit with a three-Gaussian function corresponding to pions, kaons, and protons. The corresponding widths and centroids are extracted from the data as a function of transverse momentum. In the calibration process, we ensure that the centroids of these distributions do not move as a function of p_T and that the widths vary as expected from the known momentum and timing resolution of the detector. We then select a sample from each particle species aiming for at least 90% purity in PID. The high purity of the sample will allow us to measure the v_2 of selected particles accurately and minimize the uncertainty resulting from PID contamination. At lower transverse momenta ($p_T < 2.5$ GeV/c), the 2σ bands centered around each particle's m^2 do not overlap, thus symmetric cuts, $m_0^2 - 2\sigma < m^2 < m_0^2 + 2\sigma$, allow for PID with high purity. In the range 2.5 GeV/c $< p_T <$ 3 GeV/c, the π/K separation is achieved by excluding the particles that lie within 2σ of the centroid of the mass-squared distribution of another particle. This procedure is demonstrated in Fig. 3, where the PID selections for π, K, and p are shown with the hatched areas in the plot. The Gaussian fits to the individual m^2 peaks (dashed-line curves) and the combined fit to the entire m^2 distribution (solid line) are also shown.

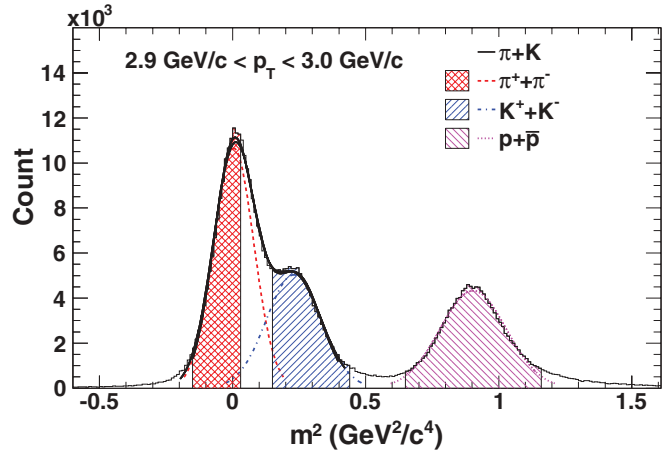

FIG. 3. (Color online) The mass-squared distribution measured by TOFw in the p_T region 2.9 GeV/c $< p_T <$ 3.0 GeV/c. The hatched areas show the pion, kaon, and proton selections, from left to right. The dashed lines show Gaussian fits to the individual m^2 peaks, while the solid line represents a combined fit to the m^2 distribution including the pions and kaons.

At higher transverse momentum 3 GeV/c $< p_T <$ 6 GeV/c, the lower m^2 range of the pion distribution remains relatively unaffected by contamination from kaons and protons. Therefore, a pion sample with purity better than 90% can be selected based on information from the TOFw alone, by applying the m^2 cuts indicated in Figs. 4(a) and 4(c) and listed in Table II.

For kaon and proton identification at $p_T > 3$ GeV/c, the ACC is used in conjunction with the TOFw detector, as shown in Figs. 4(b) and 4(d). The turn-on momenta of the ACC for

TABLE II. The particle identification cuts in TOFw and ACC with PID purity in Au + Au collisions for the centralities 0–20% and 20–60%.

Particle	p_T range	TOFw Cut	ACC Cut	Purity	
	(GeV/c)	(GeV/c^2)^2		0–20%	20–60%
pion	<3	$m_\pi^2 \pm 2\sigma_{m_\pi^2}$ veto on $m_K^2 \pm 2\sigma_{m_K^2}$	None	99%	99%
	[3.0, 5.0)	[−1.0, 0.0]	None	95%	96%
	[5.0, 6.0)	[−1.0, −0.1]	None	91%	92%
kaon	<3	$m_K^2 \pm 2\sigma_{m_K^2}$ veto on $m_\pi^2 \pm 2\sigma_{m_\pi^2}$	None	98%	99%
	[3.0, 3.5)	[0.1, 0.5]	accph < 5.0	94%	95%
	[3.5, 4.0)	[0.1, 0.5]	accph < 5.0	91%	92%
proton	<3	$m_p^2 \pm 2\sigma_{m_p^2}$	None	99%	99%
	[3.0, 4.0)	[0.6, 1.3]	accph < 5.0	97%	98%
	[4.0, 5.0)	[0.7, 1.3]	accph < 5.0	95%	96%
	[5.0, 6.0)	[0.7, 1.7]	accph < 5.0	91%	92%

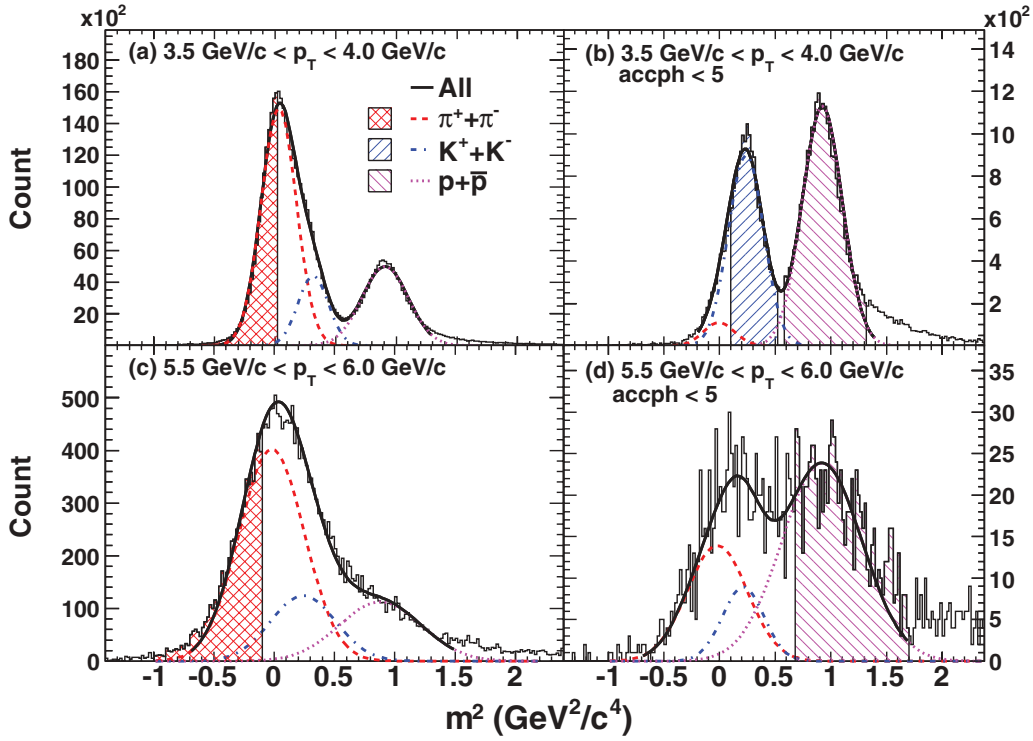

FIG. 4. (Color online) The mass-squared distribution in the TOFw without (left panels) and with (right panels) the ACC photon yield (accph) cuts for different p_T regions. The hatched areas show the m^2 cuts used for pion, kaon, and proton selections. The distribution is fit with a three-Gaussian function (solid line). The individual Gaussian distributions corresponding to π, K, and p and are as dashed lines.

pions, kaons, and protons are 1.0 GeV/c, 3.0 GeV/c, and 6.0 GeV/c, respectively. This turn-on is gradual, with the number of photons registered per photomultiplier tube (PMT) growing up to 15 for pions, and 10 (kaons and protons) as the hadrons exceed their respective threshold momentum by $\approx$1 GeV/c. With this information, the photon yield from the ACC can be used as a rejection veto based on whether it is "on" (accph $\geqslant$ 5) or "off" (accph $<$ 5). Due to the occupancy effects in the ACC as well as the spatial resolution of track projection to the ACC, the pions cannot be rejected completely. The effect of this veto cut is demonstrated in Figs. 4(b) and 4(d). The pion rejection by the ACC in combination with asymmetric m^2 cuts, which are indicated here and listed in Table II, allow for kaon and proton PID up to p_T of 4 and 6 GeV/c, respectively.

We use the Gaussian fits to the mass-squared distributions to estimate the PID purity in the selected m^2 regions. This is straightforward at $p_T < 3$ GeV/c, where the peaks associated with each particle are well defined. At higher p_T the uncertainties are larger, since the pion and kaon peaks merge and the individual yields are not well constrained. We have checked that for $p_T > 4$ GeV/c, after efficiency corrections, the K/π ratio obtained from our fits is consistent with the measurements of the K/π (K^0_S/π) ratio by the STAR experiment within the statistic and systematic uncertainties. At $p_T = 5.22$ GeV/c, the K/π ratio is reported as $0.326 \pm 0.013(\text{stat}) \pm 0.134(\text{syst})$ and the K^0_S/π ratio is reported as $0.435 \pm 0.022(\text{stat}) \pm 0.072(\text{syst})$ in $p+p$ collisions at $\sqrt{s_{NN}} = 200$ GeV; the ratios in $p+p$ and Au + Au collisions are similar [45–47]. In our study, the kaon contamination in the pion sample is relatively insensitive to the kaon yield. For example, if we artificially increase the kaon yield by 30%, the contamination in the pion sample increases from 7% to 9%.

The m^2 distributions are not strictly Gaussian shape, but have tails extending to the higher mass region. This effect is not noticeable at low p_T but comes into prominence at intermediate and high p_T. Hadrons coming from resonance decays may survive the tracking cuts but will have misreconstructed momentum and contribute to this high mass tail. Detector simulations demonstrated that the momentum distribution of hadrons, which includes the primary hadrons and those from resonance decays, is much closer to a Landau distribution at high p_T. To get a better estimate of the possible PID contamination in this case, we have fit the m^2 distribution with an empirical function that was determined by sampling a momentum distribution with a Landau shape instead of a Gaussian. This empirical m^2 distribution is found to give a much better fit than a simple three-Gaussian function and it gives a good description of the high mass tails. Finally, we reevaluate the PID contamination with this empirical function. An example of these fits is shown in Fig. 5. The tail of m^2 distribution is well described by the empirical pion, kaon, and proton m^2 functions which are presented with different dashed lines. In this case, at high p_T the contamination from kaons and pions in the proton sample increases to 9% from 1% in the case of the Gaussian fits.

The PID purity for each particle species estimated in different p_T ranges is listed in Table II. These estimates reflect the values obtained for the 0–20% central Au + Au collisions

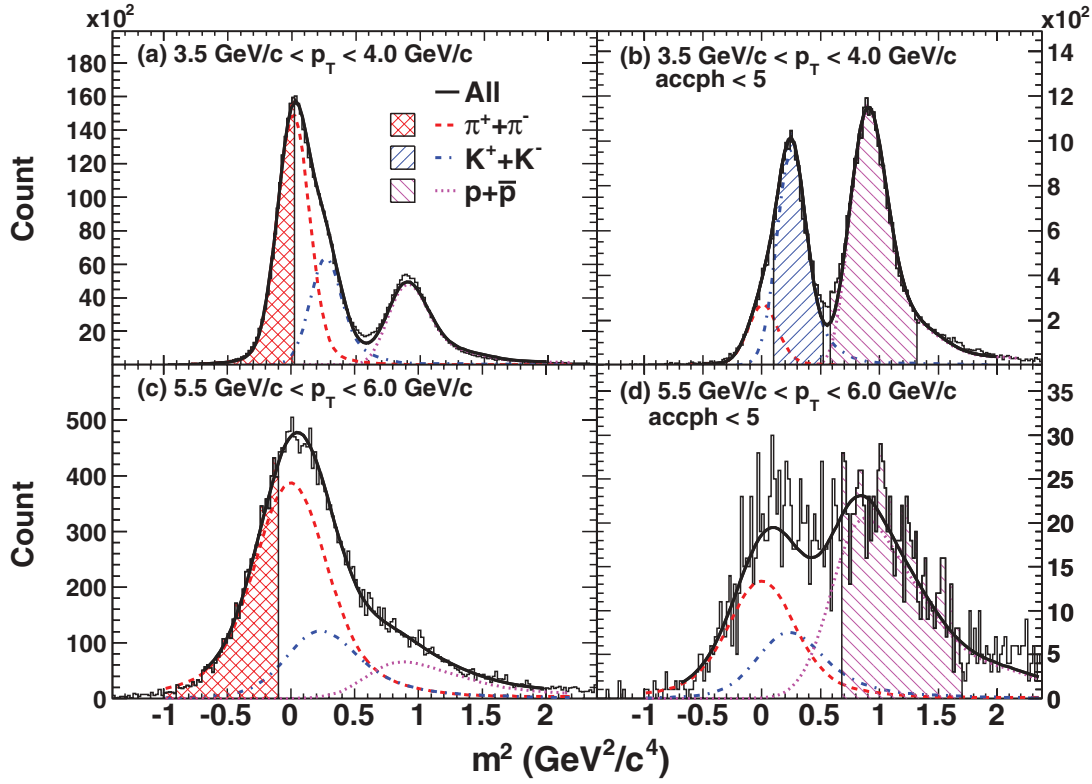

FIG. 5. (Color online) The mass-squared distribution in the TOFw without (left panels) and with (right panels) the ACC photon yield (accph) cuts for different p_T regions. The hatched areas show the m^2 cuts used for pion, kaon, and proton selections. The distribution is fit with the sum of three empirical m^2 distribution functions that are propagated from sampling a Landau shape momentum distribution as described in the text (solid line). The individual distributions corresponding to π, K, and p are shown with dashed lines.

and are meant to provide lower limits for the measurements presented here. The purity in more peripheral collisions was found to be slightly better.

C. Measurement of v_2

The measurement of the anisotropy parameter v_2 aims to determine the event-by-event particle azimuthal correlation with the reaction plane of the collision. The true reaction plane, which is defined as the plane formed by the impact parameter b and the beam direction, is not known experimentally. In addition, there exist other sources of correlations in azimuth, such as the correlations from resonance decays, jets, and Bose-Einstein effects. These correlations, which are not related to the reaction plane, are called nonflow correlations. The goal is to determine the second coefficient in the Fourier expansion v_2 of the particle azimuthal distribution with respect to the reaction plane with minimal effects from nonflow correlations. To estimate the reaction plane angle $\Psi_{\rm RP}$, we employ the event-plane method [40], in which the second harmonic azimuthal anisotropy signal determines the event-plane angle Ψ based on hits registered in one of the event-plane detectors: RxNP or MPC. For an ideal detector, the measured distribution of event-plane angles should be isotropic. However, the actual measurement is usually affected by finite acceptance and nonuniform efficiencies. We apply a standard event-plane flattening technique [16,19,40,48] to remove the residual nonuniformities in the distribution of event-plane angles. The accuracy with which the event-plane angle can be determined depends on the strength of the v_2 signal and the multiplicity of the events in each centrality class. It is maximal for midcentral events, where both of these quantities are relatively large. The $v_2(p_T)$ measurement is performed by correlating the particle azimuthal angle φ with the second harmonic event-plane angle Ψ, and correcting the observed signal for the event-plane resolution as follows:

$$v_2 = \frac{\langle \cos[2(\varphi - \Psi)] \rangle}{\mathrm{Res}(\Psi)} \tag{2}$$

Here the brackets $\langle\rangle$ indicate an average over all particles in all events.

Since the true reaction plane angle is not directly measurable, the resolution correction is estimated using subevent techniques [40]. There are several different options in using the subevent techniques. The present analysis uses the two subevent and the three subevent methods. These methods are compared to evaluate the systematic uncertainties associated with the event-plane resolution corrections.

The RxNP and the MPC detectors each have two subdetectors, North and South, which are positioned symmetrically around the origin of the nominal collision point with equal acceptance in pseudorapidity. Thus, they provide a natural two-subevent division. The correlation between the event-plane angles determined from the North and South subdetectors, Ψ_N

and Ψ_S, allows for the estimate of the resolutions corrections as follows:

$$\mathrm{Res}(\Psi_N) = \mathrm{Res}(\Psi_S) = \sqrt{\langle \cos 2(\Psi_S - \Psi_N)\rangle}. \quad (3)$$

The resolution correction can also be expressed analytically [40] as

$$\mathrm{Res}(\Psi) = \langle \cos 2(\Psi - \Psi_{\mathrm{RP}})\rangle = \frac{\sqrt{\pi}}{2}\chi e^{-\frac{\chi^2}{2}}\left[I_0\left(\frac{\chi^2}{2}\right) + I_1\left(\frac{\chi^2}{2}\right)\right], \quad (4)$$

where I_0 and I_1 are modified Bessel functions. The parameter $\chi = v_2\sqrt{2M}$, where M is the number of particles used to determine the event plane, describes the dispersion of the flow vector. With the use of Eqs. (3) and (4), we obtain the subevent parameters χ_S and χ_N. Subsequently, to optimize the event-plane resolution, the two subevents are combined, and the full event parameter is taken as $\chi = \sqrt{2}\chi_S = \sqrt{2}\chi_N$. This procedure relies on the two subevents being equal in multiplicity and registering the same size v_2 signal, which may not be the case experimentally. To avoid this uncertainty, we also use a three-subevents technique to determine the event-plane resolution with Eq. (5) [40]. To determine the event-plane resolution of RxNP detector (subevent A), we employ information from the North and South portions of the MPC detector (subevents B and C). In turn, to estimate the resolution of the MPC detector, the North and South portions of the RxNP detector are used to provide subevents B and C,

$$\mathrm{Res}(\Psi_A) = \langle \cos 2(\Psi_A - \Psi_{\mathrm{RP}})\rangle = \sqrt{\frac{\langle \cos 2(\Psi_A - \Psi_B)\rangle \langle \cos 2(\Psi_A - \Psi_C)\rangle}{\langle \cos 2(\Psi_B - \Psi_C)\rangle}}. \quad (5)$$

The event-plane resolution for the RxNP (circles) and the MPC (triangles) detectors obtained with the above procedures are shown as a function of the event centrality in Fig. 6(a). The results show the expected trend, with maximal resolution for the 20–30% centrality class where both the event multiplicity and the v_2 signal are large, and a decrease for the more central events (due to lower v_2 strength), and more peripheral events (due to smaller multiplicity). Figure 6(b) shows the ratio of the results obtained with the two-subevent and the three-subevent techniques. The results for the RxNP detector (closed symbols) agree to within 2%. A larger difference (up to 4%) is observed for the MPC detector (open symbols), which is mainly due to the asymmetric pseudorapidity coverage of the MPC. The event-plane resolution from three-subevents method is used to correct the v_2 measurement.

From Fig. 6 it is evident that the RxNP detector has better resolution for the event-plane angle, as well as smaller systematic uncertainty in the event-plane determination than the MPC detector. Therefore, it is desirable to use the RxNP for the v_2 measurement. One possible disadvantage of the RxNP over the MPC detector is the smaller pseudorapidity separation from the central spectrometer ($|\eta| < 0.35$), which makes the v_2 measurement more susceptible to nonflow correlations caused by jets. Since the results presented here aim to study the high p_T azimuthal anisotropies of identified charged hadrons and the limits of n_q scaling, it is particularly important to minimize

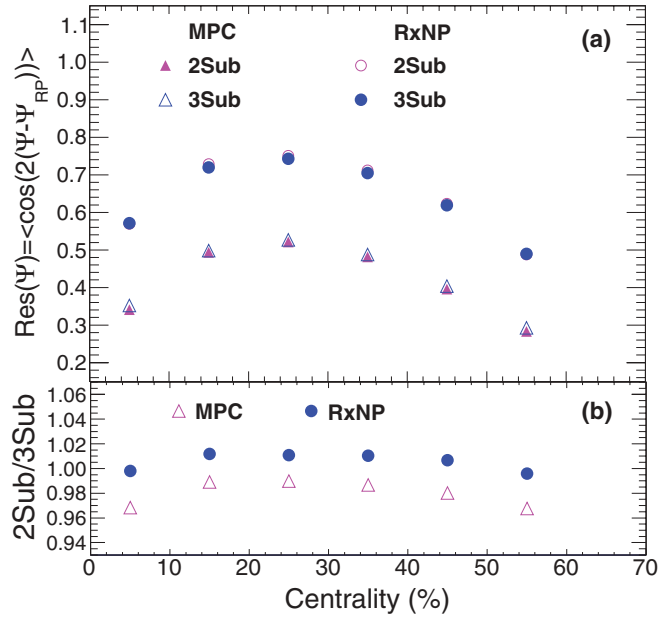

FIG. 6. (Color online) Panel (a) shows the event-plane resolution as a function of centrality for the RxNP and the MPC detectors. Panel (b) shows the ratio of the event-plane resolution obtained from two subevents and three subevents as a function of centrality.

such effects. To evaluate the nonflow contributions we examine the $v_2(p_T)$ distributions for pions, kaons, and protons measured using the MPC and the RxNP detectors independently. For the $p_T < 6$ GeV/c, a previous study indicated that nonflow effects are small for the event plane measured by the BBC detectors, which have a pseudorapidity coverage similar to that of the MPC detectors [49]. Figure 7 shows the results in the 0–60% centrality range for each particle species (upper panels), and the ratio of the results obtained with the two event-plane detectors (lower panels). Nonflow correlations are expected to enhance the measured v_2 signal for the detector that is more affected, especially in the higher p_T range. We do not find any evidence for a significant increase in nonflow contributions in the measurement based on the RxNP detector.

Based on these considerations, the results presented in Sec. IV are based on the reaction plane measured solely by the RxNP, taking advantage of its better event-plane resolution in comparison to the MPC.

D. Systematic uncertainties in v_2

The systematic uncertainties in the v_2 measurement obtained with the RxNP detector can be broadly characterized according to the following categories: (i) event-plane resolution corrections; (ii) event-plane measured from different detectors; (iii) v_2 from background tracks; (iv) PID purity; and (v) acceptance and run-by-run dependencies.

The uncertainties stemming from the event-plane resolution corrections are independent of particle species and p_T. They are found to be around 2% for all centralities by studying the event-plane resolution difference for the RxNP with the two- and three-subevent methods.

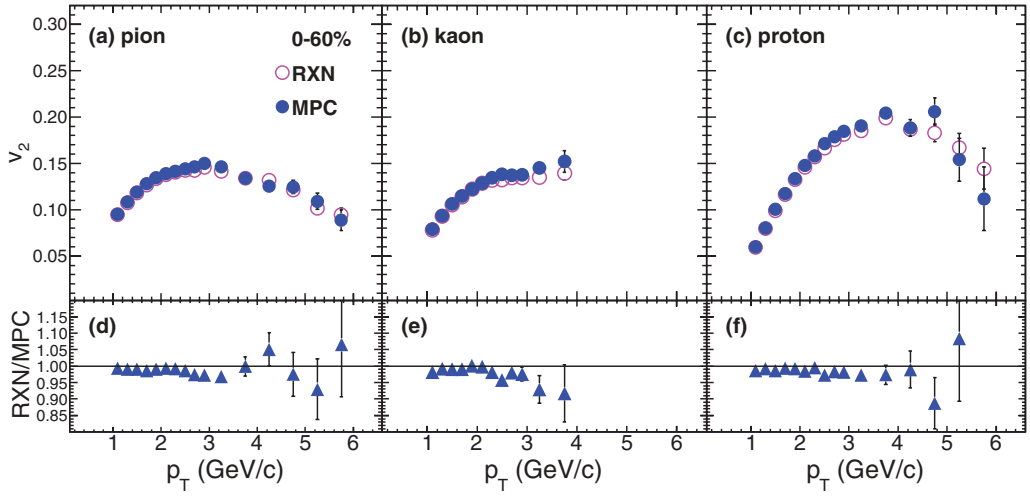

FIG. 7. (Color online) The upper panels show the azimuthal anisotropy $v_2(p_T)$ of pions (a), kaons (b), and protons (c) in the 0–60% centrality class measured with respect to event planes determined by the MPC (closed symbols) or the RxNP (open symbols) detectors. The event-plane resolution is estimated by the three-subevents method. The ratio of v_2(RxNP) to v_2(MPC) is shown in the lower panels as a function of p_T for pions (d), kaons (e), and protons (f).

The uncertainties from event planes measured with different detectors (RxNP, MPC) are found to be independent of the particle species, by comparing the results from RxNP and MPC. In the 0–20% centrality class, we assign a 3% systematic uncertainty for $p_T < 3$ GeV/c and a 5% systematic uncertainty for $p_T > 3$ GeV/c. In the 20–60% centrality class, we assign a 3% systematic uncertainty for $p_T < 5$ GeV/c and a 5% systematic uncertainty for $p_T > 5$ GeV/c.

Background tracks that are not removed by the tracking and PID selections outlined in Secs. III A and III B may influence the measured v_2 if they carry a signal that is different from the particle of interest. The background tracks may come from decays, γ conversions, or false track reconstruction. The backgrounds are centrality dependent, and may also have p_T and hadron species dependence. A sample of background-dominated tracks was selected based on the normalized distance between the hits registered in the TOFw detector and the track projections. Specifically, a 4σ–10σ window in the z direction was utilized. The azimuthal anisotropy of the background was then measured following the procedure used for the signal. For $p_T \approx 3$ GeV/c, the v_2 of the background is similar to that of the pion, but it decreases at higher p_T down to about 60% of the v_2 of the pion (or 30% of the v_2 of the proton) for $p_T \approx 6$ GeV/c in the 0–20% centrality class. For pions, the resulting systematic uncertainties in v_2 are of the order 1% for $p_T < 4$ GeV/c and reach up to 4% (3%) for $p_T \approx 6$ GeV/c for centrality 0–20% (20–60%). For protons, the resulting systematic uncertainties in v_2 are of the order 1% for $p_T < 4$ GeV/c and reach up to 5% (3%) for $p_T \approx 6$ GeV/c for centrality 0–20% (20–60%).

TABLE III. Systematic uncertainties given in percent on the v_2 measurements.

Error Sources	Species	0–20%	20–60%	Type
Event-plane resolution		2%	2%	C
Event-plane detectors		3% in p_T 1–3 GeV/c	3% in p_T 1–5 GeV/c	B
		5% in p_T 3–6 GeV/c	5% in p_T 5–6 GeV/c	
Background	pion	1% in p_T 1–4 GeV/c	1% in p_T 1–4 GeV/c	A
		4% in p_T 4–6 GeV/c	3% in p_T 4–6 GeV/c	
	kaon	1% in p_T 1–4 GeV/c	1% in p_T 1–4 GeV/c	A
	proton	1% in p_T 1–4 GeV/c	1% in p_T 1–4 GeV/c	A
		5% in p_T 4–6 GeV/c	3% in p_T 4–6 GeV/c	
PID	pion	negligible in p_T 1–3 GeV/c		A
		2% in p_T 3–6 GeV/c		
	kaon	negligible in p_T 1–3GeV/c		A
		2% in p_T 3–4 GeV/c		
	proton	negligible in p_T 1–3 GeV/c		A
		3% in p_T 3–4 GeV/c	2% in p_T 3–4 GeV/c	
		5% in p_T 4–6 GeV/c	3% in p_T 4–6 GeV/c	
Acceptance and run-by-run		8%	3%	C

The systematic uncertainties in v_2 resulting from hadron misidentification are based on the PID purity estimates listed in Table II and the size of v_2 of each species. For example, at $p_T = 6.0$ GeV/c for 0–20% centrality, the protons purity is around 91% and the v_2 of pions and kaons are around 50% of that of the proton. We assign a 5% systematic uncertainty attributable to this effect. For $p_T < 3$ GeV/c, the uncertainties in v_2 due to PID contamination are negligible for all particle species. At higher p_T the uncertainties in v_2 remain below $\approx 2\%$ for kaons and pions; for protons with $p_T > 4$ GeV/c these uncertainties reach up to $\approx$5% (3%) for centrality 0–20% (20–60%).

Additional systematic checks were performed using different subsets of the detector, and data obtained with different magnetic field configurations. Differences of order 8% (3%) were found for the 0–20% (20–60%) centrality, which have weak p_T and particle species dependence.

Table III lists the summary of all these systematic uncertainties, which are categorized by the types:

(A) point-to-point error uncorrelated between p_T bins,
(B) p_T correlated, all points move in the same direction but not by the same factor,
(C) an overall normalization error in which all points move by the same factor independent of p_T.

IV. RESULTS AND DISCUSSION

The results for v_2 of identified pions, kaons, and protons are presented in Fig. 8; the results in central collisions (0–20%) are presented in Figs. 8(a), 8(c), and 8(e) and the results in noncentral collisions (20–60%) are presented in Figs. 8(b), 8(d), and 8(f). The symbols representing the different particle species are closed triangles for pions, open squares for kaons, and closed circles for protons. In order to better compare between two centralities, the v_2 of all species in the 0–20% centrality has been scaled up by a factor of 1.6. The error bars (shaded boxes) represent the statistical (systematic) uncertainties. The systematic uncertainties shown are type A and B only. Not shown are the type C systematic uncertainties, which are from the event-plane resolution, geometrical acceptance, and run-by-run dependence are around 8.5% (3.5%) for 0–20% (20–60%) centrality for all species at all values of p_T.

Figures 8(a) and 8(b) show $v_2(p_T)$. For both centrality selections, the v_2 values of pions and kaons are very similar in intermediate p_T range (2–4 GeV/c), where the measured v_2 is maximal and is relatively independent of transverse momentum. Above $p_T \approx 4$ GeV/c the pion v_2 gradually decreases to a value which is comparable to the signal measured at $p_T \approx 1$ GeV/c. In contrast, the proton $v_2(p_T)$ has a shape that is centrality dependent. In central collisions (0–20%) the proton v_2 rises up to $p_T \approx 3.5$ GeV/c and then saturates at a value higher than the v_2 of pions. For noncentral collisions, the behavior is different: a decrease is observed in the proton v_2 for $p_T > 4$ GeV/c leading to near equal v_2 signals for pions and protons at $p_T \approx 6$ GeV/c.

The use of the KE_T variable was introduced in Ref. [18], which is found to better represent the number of quark scaling behavior than p_T at lower p_T. In Figs. 8(c) and 8(d) the v_2 signals have been scaled by the number of constituent quarks

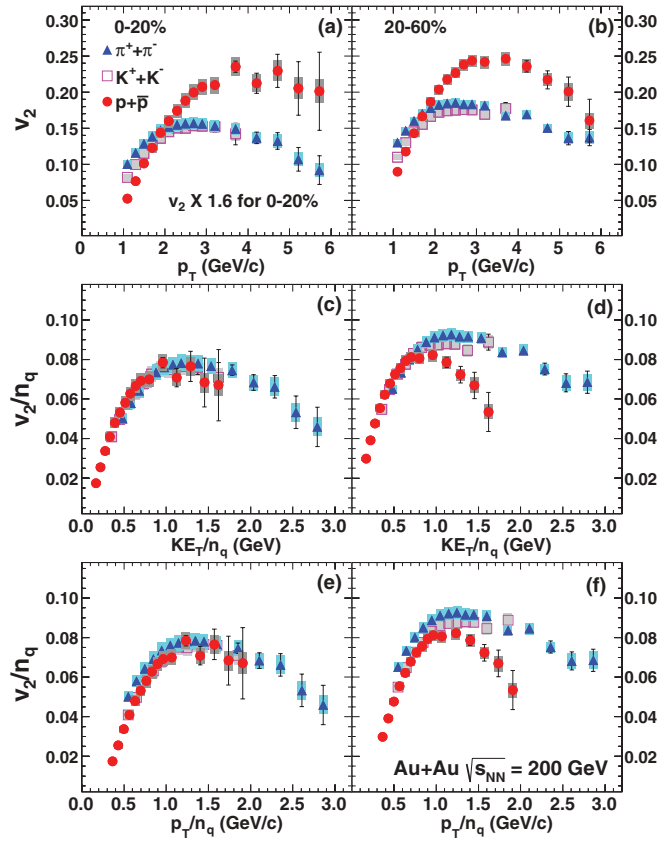

FIG. 8. (Color online) Identified hadron v_2 in central (0–20% centrality, left panels) and midcentral (20–60%, right panels) Au + Au collisions at $\sqrt{s_{NN}} = 200$ GeV. Panels (a) and (b) show v_2 as a function of transverse momentum p_T. Panels (c) and (d) show the quark-number-scaled v_2 (v_2/n_q) as a function of the kinetic energy per quark, KE_T/n_q. Panels (e) and (f) show v_2/n_q as a function of transverse momentum per quark, p_T/n_q. The v_2 of all species for centrality 0–20% has been scaled up by a factor of 1.6 for better comparison with results of 20–60% centrality. The error bars (shaded boxes) represent the statistical (systematic) uncertainties. The systematic uncertainties shown are type A and B only.

n_q in the hadrons and are shown as a function of the transverse kinetic energy per quark KE_T/n_q. A very different behavior is observed in central [Fig. 8(c)] and in noncentral [Fig. 8(d)] collisions. In the measured p_T range, a universal behavior is seen in the central collisions within the statistical and systematic uncertainties, but not in the noncentral collisions, where the v_2/n_q of protons falls below that of the mesons for $\mathrm{KE}_T/n_q \geqslant 1$ GeV. This is the range where the proton $v_2(p_T)$ begins falling in noncentral collisions but remains relatively constant in central collisions.

On the other hand, it is widely accepted that the relevant scaling variable for quark recombination is the transverse momentum per quark, since it is the momentum and not the energy that is additive in the recombination models. Therefore, to examine the n_q scaling in the recombination regime we show the quark-number-scaled v_2 as a function of p_T/n_q in Figs. 8(e) and 8(f). For central collisions [Fig. 8(e)], the universal behavior appears to remains valid within the

statistical and systematic uncertainties. Since the changes in v_2 are relatively small at higher p_T, shifting the x axis from KE_T/n_q to p_T/n_q does not change the shape of the curves significantly. For noncentral collisions [Fig. 8(f)], the proton data are systematically below the pion data at all p_T/n_q, although they are at the edge of the systematic uncertainties for $p_T/n_q \leqslant 1.3$ GeV/c, which corresponds to $\mathrm{KE}_T/n_q \leqslant 1$ GeV/c. We note that despite this systematic offset, the n_q scaling makes the shape of the pion and proton curves very similar below the breaking point. Above that point, quark recombination is clearly violated.

Some model calculations [30] have shown that the breaking of n_q scaling occurs at the transition between purely thermal and thermal+shower recombination. In the 50–60% centrality class this can happen for values of KE_T as low as $\mathrm{KE}_T/n_q \approx 0.5$ GeV, while in the 0–5% centrality class this occurs at values as high as $\mathrm{KE}_T/n_q \approx 1.5$ GeV. Similar features have been observed in the data presented in this paper. On the other hand, for pions and protons, the nuclear modification factors (R_{AA}), which are used to quantify the amount of partonic energy loss in the medium, have been found to be consistent with each other for $p_T > 5$ GeV/c [47,50–52]. This indicates that a simple interplay between recombination and jet energy loss is not enough to explain the v_2 and R_{AA} of pions and protons in Au + Au collisions in this p_T region. Additional considerations may include the non-Abelian nature of jet energy loss [53], the quark versus gluon fragmentation production of pions and protons [54–56], and jet chemistry effects such as enhanced parton splitting [57] and jet conversion [58]. Detailed model calculations that take all of these effects into account are not yet available, and it is an open question whether doing so is enough for an adequate interpretation of the p_T v_2 and R_{AA} of pions and protons.

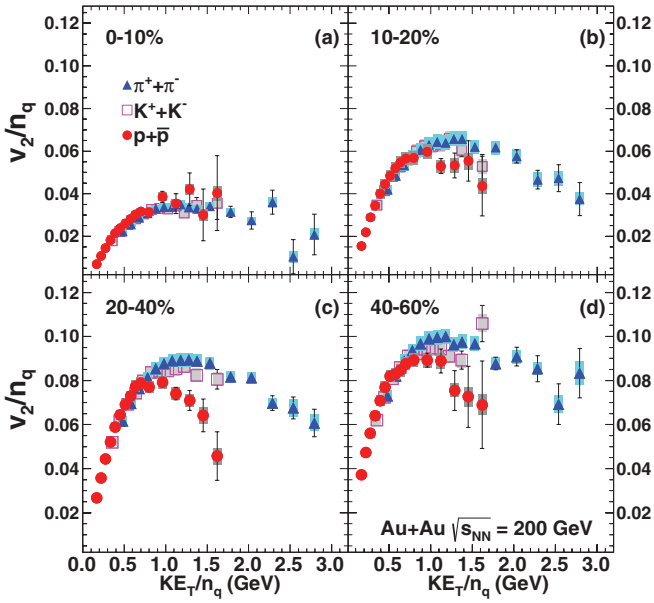

FIG. 9. (Color online) The quark-number-scaled v_2 (v_2/n_q) of identified hadrons are shown as a function of the kinetic energy per quark, KE_T/n_q in 0–10% centrality [panel (a)], 10–20% [panel (b)], 20–40% [panel (c)], and 40–60% centrality [panel (d)] in Au + Au collisions at $\sqrt{s_{NN}} = 200$ GeV. The error bars (shaded boxes) represent the statistical (systematic) uncertainties. The systematic uncertainties shown are type A and B only.

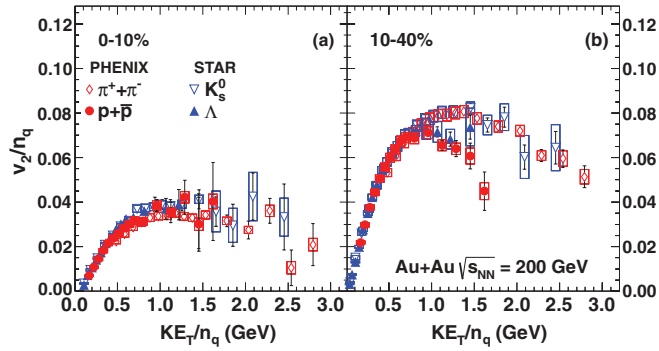

FIG. 10. (Color online) The quark-number-scaled v_2 (v_2/n_q) of identified hadrons are shown as a function of the kinetic energy per quark, KE_T/n_q in 0–10% centrality [panel (a)] and 10–40% centrality [panel (b)] in Au + Au collisions at $\sqrt{s_{NN}} = 200$ GeV. The v_2 of Λ and K^0_S are measured by STAR collaboration [21]. The error bars (open boxes) represent the statistical (systematic) uncertainties. The systematic uncertainties shown on the results from this study are type A and B only.

To further investigate the centrality dependence of the n_q scaling breaking, results with finer centrality bins are shown in Fig. 9. The quark number scaled v_2 (v_2/n_q) of pions, kaons, and protons are shown as a function of the kinetic energy per quark KE_T/n_q in 0–10% [Fig. 9(a)], 10–20% [Fig. 9(b)], 20–40% [Fig. 9(c)], and 40–60% centrality [Fig. 9(d)]. The error bars (shaded boxes) represent the statistical (systematic) uncertainties. The systematic uncertainties shown are type A and B only. Not shown are the type C systematic uncertainties, which are from the event-plane resolution, geometrical acceptance, and run-by-run dependence, and are around 10.5% (3.5%) for 0–10% (40–60%). These results with finer centrality bins show that the breaking of n_q scaling has a clear centrality dependence.

We also compare our results with the existing v_2 results for K^0_S and Λ as measured by the STAR collaboration using the event-plane method [21] in the 0–10% and 10–40% centrality classes, which are shown in Figs. 10(a) and 10(b), respectively. Since the event plane and particles are measured in the same rapidity gap by the STAR detector in their event-plane method, the v_2 values from STAR measurements are expected to be systematically larger than those measured by PHENIX [21,48] due to nonflow effects. In the 0–10% centrality class, the v_2 of pions and protons in this study are systematically lower than the v_2 of K^0_S and Λ by 17% independent of p_T, but they are within the systematic uncertainties. The n_q scaling appears to hold in this centrality class for each particle species. In the 10–40% centrality class, the v_2 of pions and protons are consistent with that of K^0_S and Λ in the overlapping KE_T region. While the presence of the scaling breaking is not clear in the K^0_S and Λ results, the improved precision and extended KE_T reach of the present study unambiguously demonstrates the breaking of n_q scaling in this centrality class.

V. SUMMARY AND CONCLUSION

We have presented a high-statistics study of baryon and meson azimuthal anisotropy v_2 measured up to p_T of 6 GeV/c as a function of centrality in $\sqrt{s_{NN}} = 200$ GeV Au + Au collisions. The n_q scaling is found to exhibit strong dependence on the collision centrality. Significant deviations from n_q scaling are found in noncentral collisions, starting from the 10–20% centrality class, as $\mathrm{KE}_T/n_q > 0.7$ GeV. These results indicate that particle production above $p_T \approx 2$ GeV/c is not dominated by recombination, but that other mechanisms—such as parton-energy loss, jet chemistry, and different fragmentation functions—may contribute to generating the azimuthal anisotropy of particle emission. Conversely, in central collisions, such as for 0–10% centrality, the universal n_q scaling appears to hold to $\mathrm{KE}_T/n_q = 1.5$ GeV. This observation supports parton recombination as the dominant mode of particle production at intermediate transverse momentum in central Au + Au collisions at top RHIC energy.

ACKNOWLEDGMENTS

We thank the staff of the Collider-Accelerator and Physics Departments at Brookhaven National Laboratory and the staff of the other PHENIX participating institutions for their vital contributions. We acknowledge support from the Office of Nuclear Physics in the Office of Science of the Department of Energy, the National Science Foundation, Abilene Christian University Research Council, Research Foundation of SUNY, and Dean of the College of Arts and Sciences, Vanderbilt University (USA), Ministry of Education, Culture, Sports, Science, and Technology and the Japan Society for the Promotion of Science (Japan), Conselho Nacional de Desenvolvimento Científico e Tecnológico and Fundação de Amparo à Pesquisa do Estado de São Paulo (Brazil), Natural Science Foundation of China (People's Republic of China), Ministry of Education, Youth and Sports (Czech Republic), Centre National de la Recherche Scientifique, Commissariat à l'Énergie Atomique, and Institut National de Physique Nucléaire et de Physique des Particules (France), Bundesministerium für Bildung und Forschung, Deutscher Akademischer Austausch Dienst, and Alexander von Humboldt Stiftung (Germany), Hungarian National Science Fund, OTKA (Hungary), Department of Atomic Energy and Department of Science and Technology (India), Israel Science Foundation (Israel), National Research Foundation and WCU program of the Ministry Education Science and Technology (Korea), Ministry of Education and Science, Russian Academy of Sciences, Federal Agency of Atomic Energy (Russia), VR and the Wallenberg Foundation (Sweden), the US Civilian Research and Development Foundation for the Independent States of the Former Soviet Union, the US-Hungarian Fulbright Foundation for Educational Exchange, and the US-Israel Binational Science Foundation.

[1] K. Adcox *et al.* (PHENIX Collaboration), Nucl. Phys. A **757**, 184 (2005).
[2] J. Adams *et al.* (STAR Collaboration), Nucl. Phys. A **757**, 102 (2005).
[3] B. B. Back *et al.* (PHOBOS Collaboration), Nucl. Phys. A **757**, 28 (2005).
[4] I. Arsene *et al.* (BRAHMS Collaboration), Nucl. Phys. A **757**, 1 (2005).
[5] E. V. Shuryak, Nucl. Phys. A **750**, 64 (2005).
[6] M. Gyulassy and L. McLerran, Nucl. Phys. A **750**, 30 (2005).
[7] U. Heinz, in *Relativistic Heavy Ion Physics*, Landolt-Boernstein New Series, edited by R. Stock, Vol. I/23 (Springer Verlag, New York, 2010), Chap. 5.
[8] P. Romatschke, Int. J. Mod. Phys. E **19**, 1 (2010).
[9] D. A. Teaney, in *Quark-Gluon Plasma 4*, edited by R. C. Hwa and X. N. Wang (World Scientific, Singapore, 2010), p. 207.
[10] P. K. Kovtun, D. T. Son, and A. O. Starinets, Phys. Rev. Lett. **94**, 111601 (2005).
[11] S. S. Adler *et al.* (PHENIX Collaboration), Phys. Rev. C **76**, 034904 (2007).
[12] S. Afanasiev *et al.* (PHENIX Collaboration), Phys. Rev. C **80**, 054907 (2009).
[13] A. Adare *et al.* (PHENIX Collaboration), Phys. Rev. Lett. **105**, 142301 (2010).
[14] S. A. Bass, C. Gale, A. Majumder, C. Nonaka, G.-Y. Qin, T. Renk, and J. Ruppert, Phys. Rev. C **79**, 024901 (2009).
[15] X. N. Wang, Phys. Rev. C **63**, 054902 (2001).
[16] S. S. Adler *et al.* (PHENIX Collaboration), Phys. Rev. Lett. **91**, 182301 (2003).
[17] J. Adams *et al.* (STAR Collaboration), Phys. Rev. Lett. **92**, 052302 (2004).
[18] A. Adare *et al.* (STAR Collaboration), Phys. Rev. Lett. **98**, 162301 (2007).
[19] S. Afanasiev *et al.* (STAR Collaboration), Phys. Rev. Lett. **99**, 052301 (2007).
[20] B. Abelev *et al.* (STAR Collaboration), Phys. Rev. C **75**, 054906 (2007).
[21] B. Abelev *et al.* (STAR Collaboration), Phys. Rev. C **77**, 054901 (2008).
[22] R. C. Hwa and C. B. Yang, Phys. Rev. C **67**, 034902 (2003).
[23] R. J. Fries, B. Muller, C. Nonaka, and S. A. Bass, Phys. Rev. Lett. **90**, 202303 (2003).
[24] R. J. Fries, B. Muller, C. Nonaka, and S. A. Bass, Phys. Rev. C **68**, 044902 (2003).
[25] V. Greco, C. M. Ko, and P. Levai, Phys. Rev. Lett. **90**, 202302 (2003).
[26] D. Molnar and S. A. Voloshin, Phys. Rev. Lett. **91**, 092301 (2003).
[27] S. S. Adler *et al.* (PHENIX Collaboration), Phys. Rev. Lett. **91**, 172301 (2003).
[28] S. S. Adler *et al.* (PHENIX Collaboration), Phys. Rev. C **69**, 034909 (2004).
[29] B. Muller, R. J. Fries, and S. A. Bass, Phys. Lett. B **618**, 77 (2005).
[30] C. B. Chiu, R. C. Hwa, and C. B. Yang, Phys. Rev. C **78**, 044903 (2008).
[31] G. Ferini, M. Colonna, M. Di Toro, and V. Greco, Phys. Lett. B **670**, 325 (2009).

[32] K. Dusling, G. D. Moore, and D. Teaney, Phys. Rev. C **81**, 034907 (2010).
[33] R. A. Lacey, A. Taranenko, R. Wei, N. Ajitanand, J. Alexander *et al.*, Phys. Rev. C **82**, 034910 (2010).
[34] O. Fochler, Z. Xu, and C. Greiner, Phys. Rev. Lett. **102**, 202301 (2009).
[35] R. A. Lacey, N. N. Ajitanand, J. M. Alexander, X. Gong, J. Jia, A. Taranenko, and R. Wei, Phys. Rev. C **80**, 051901 (2009).
[36] T. Hirano and Y. Nara, Phys. Rev. C **69**, 034908 (2004).
[37] J. C. Dunlop, M. A. Lisa, and P. Sorensen, Phys. Rev. C **84**, 044914 (2011).
[38] K. Adcox *et al.* (PHENIX Collaboration), Nucl. Instrum. Methods Phys. Res., Sect. A **499**, 469 (2003).
[39] E. Richardson *et al.* (PHENIX Collaboration), Nucl. Instrum. Methods Phys. Res., Sect. A **636**, 99 (2011).
[40] A. M. Poskanzer and S. A. Voloshin, Phys. Rev. C **58**, 1671 (1998).
[41] M. Chiu (PHENIX Collaboration) AIP Conf. Proc. **915**, 539 (2007).
[42] S. Aronson *et al.* (PHENIX Collaboration), Nucl. Instrum. Methods Phys. Res., Sect. A **499**, 480 (2003).
[43] B. Bonner *et al.*, Nucl. Instrum. Methods Phys. Res., Sect. A **508**, 181 (2003).
[44] W. J. Llope *et al.*, Nucl. Instrum. Methods Phys. Res., Sect. A **596**, 430 (2008).
[45] J. Adams *et al.* (STAR Collaboration), Phys. Rev. Lett. **92**, 052302 (2004).
[46] J. Adams *et al.* (STAR Collaboration), submitted to Phys. Rev. C arXiv:nucl-ex/0601042.
[47] G. Agakishiev *et al.* (STAR Collaboration), Phys. Rev. Lett. **108**, 072302 (2012).
[48] S. S. Adler *et al.* (PHENIX Collaboration), Phys. Rev. Lett. **96**, 032302 (2006).
[49] S. Afanasiev *et al.* (PHENIX Collaboration), Phys. Rev. C **80**, 024909 (2009).
[50] B. I. Abelev *et al.* (STAR Collaboration), Phys. Rev. Lett. **97**, 152301 (2006).
[51] A. Adare *et al.* (PHENIX Collaboration), Phys. Rev. C **83**, 064903 (2011).
[52] R. Belmont (PHENIX Collaboration) Nucl. Phys. A **830**, 697c (2009).
[53] X. N. Wang, Phys. Rev. C **58**, 2321 (1998).
[54] S. Albino, B. A. Kniehl, and G. Kramer, Nucl. Phys. B **725**, 181 (2005).
[55] S. Albino, B. A. Kniehl, and G. Kramer, Nucl. Phys. B **803**, 42 (2008).
[56] D. de Florian, R. Sassot, and M. Stratmann, Phys. Rev. D **76**, 074033 (2007).
[57] S. Sapeta and U. A. Wiedemann, Eur. Phys. J. C **55**, 293 (2008).
[58] W. Liu and R. J. Fries, Phys. Rev. C **77**, 054902 (2008).